PHYSICAL REVIEW B **93**, 165408 (2016)

# Temperature- and potential-dependent structure of the mercury-electrolyte interface

Benjamin Runge,[1] Sven Festersen,[1] Christian T. Koops,[1] Annika Elsen,[1] Moshe Deutsch,[2] Benjamin M. Ocko,[3,*]
Oliver H. Seeck,[4] Bridget M. Murphy,[1,5,†] and Olaf M. Magnussen[1,5]
[1]*Institute for Experimental and Applied Physics, CAU, Kiel, Germany*
[2]*Physics Department and Institute of Nanotechnology and Advanced Materials, Bar-Ilan University, Ramat-Gan, Israel*
[3]*Condensed Matter Physics & Materials Sciences Department, Brookhaven National Laboratory, New York, USA*
[4]*Deutsches Elektronen-Synchrotron DESY, Hamburg, Germany*
[5]*Ruprecht Haensel Laboratory, CAU, Kiel, Germany*

(Received 16 December 2015; revised manuscript received 14 March 2016; published 7 April 2016)

The atomic-scale structure of the mercury-electrolyte (0.01 M NaF) interface was studied as a function of temperature and potential by x-ray reflectivity and x-ray diffuse scattering measurements. The capillary wave contribution is determined and removed from the data, giving access to the intrinsic surface-normal electron density profile at the interface, especially to the surface layering in the Hg phase. A temperature dependent roughness anomaly known from the Hg-air interface is found to persist also at the Hg-electrolyte interface. Additionally, a temperature dependence of the layering period was discovered. The increase in the layer spacing with increasing temperature is approximately four times lager than the increase expected from thermal expansion. Finally, the interface is found to broaden towards the electrolyte side as the potential becomes more negative, in agreement with the Schmickler-Henderson theory. Our results favor a model for the interface structure, which is different to the model formerly used in comparable studies.

DOI: 10.1103/PhysRevB.93.165408

## I. INTRODUCTION

Mercury is a member of the fascinating group of liquid metals, which melt at or slightly above room temperature [1]. As all liquids, their surfaces are decorated by thermally excited capillary waves (CW). In addition to being metallic conductors, liquid metals stand out from most simple liquids by exhibiting an intriguing characteristic structure near the surface, in which the atoms are stratified in atomic layers with a periodicity $d$. The layering diminishes exponentially with depth below the interface with a decay length $\xi$.

The first theoretical models argued that the special nature of liquid metals, which can be viewed as a two-fluid system composed of charged ions and conduction electrons, is responsible for this phenomenon. The inherent abrupt change in electron density at the surface acts as a confining wall, which induces the layering [2]. This surface layering was first verified experimentally at the liquid-air interfaces of Hg [3] and Ga [4] by x-ray reflectivity (XRR) measurements. Subsequent experimental studies demonstrated such layering also for numerous other liquid metals [4–9] and liquid metal alloys [10–15].

Although Hg was the first liquid metal to experimentally exhibit layering, its surface structure remains anomalous among the many liquid metal systems studied to date, and is still not fully understood. In addition to the quasi-Bragg peak due to layering, XRR of the liquid Hg-air interface exhibits an anomalous intensity dip at lower scattering vectors and the surface roughness is found to grow with temperature faster than the prediction of CW theory [16], which describes well the thermal behavior of the liquid metal-air interface of Ga [17] and of all other liquid metals studied to date [18]. The Hg-electrolyte interface also exhibits anomalies. The additional intensity dip found at the Hg-air interface was observed to persist at the Hg-electrolyte interface as well [19,20]. Moreover, the potential dependent roughness of that interface exhibits a minimum, which is shifted relative to the position predicted by CW theory [19]. The Hg-electrolyte interface is a central model system in interfacial electrochemistry and played a major role in the development of the theory of the electrochemical double layer [21–24]. Because this liquid-liquid system provides an atomically smooth, defect-free interface, it remains of considerable importance for fundamental studies of electrochemical interfaces and adsorption phenomena, both from experimental and theoretical points of view. For example, the Hg-electrolyte system allows the growth of group-IV semiconductors [25] or single-unit-cell-thick crystalline adlayers [26] on its interface. However, x-ray scattering experiments on liquid-liquid interfaces are experimentally very challenging and data on the atomic-scale structure of these interfaces is still scarce. The few previous studies of the Hg-electrolyte interface [19,26] determined only the mean structure, and although the anomaly in the potential dependence of the interface roughness was noted, it was not studied in detail.

Thus, open questions remain concerning the anomalies discussed above. These include: Are the two phenomena at the Hg-air surface, the dip in the XRR and the deviant temperature dependent roughness, related to each other and to the Hg surface tension and how? Does the anomalous temperature dependence of the Hg-air interface roughness persist also at the Hg-electrolyte interface? If yes, is it related to the anomalous potential dependence, and how?

To gain insight into these issues, we carried out a detailed experimental study of the temperature and potential dependent structure of the interface between liquid Hg and an aqueous sodium fluoride (0.01 M) solution. The interface-normal

---

[*] Present address: NSLS-II, Brookhaven National Laboratory, Upton, NY 11973, USA.

[†] murphy@physik.uni-kiel.de

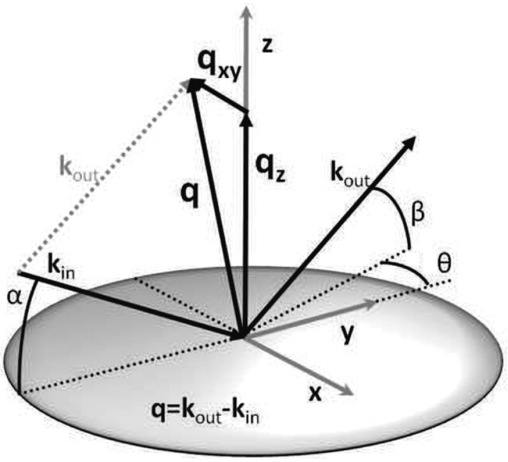

FIG. 1. Scattering geometry. $\mathbf{k}_{\rm in}$ and $\mathbf{k}_{\rm out}$ are the wave vectors of the incoming and scattered x rays. $\alpha$ and $\beta$ are the incidence and exiting angles. $\theta$ is the azimuthal angle. Specular intensity is collected at $\theta = 0$, $\alpha = \beta$, background intensity at $\alpha = \beta$, $\theta = 0$. $\mathbf{q}_z$ [with magnitude $q_z = \frac{2\pi}{\lambda}(\sin(\alpha) + \sin(\beta))$] is the orthogonal and $\mathbf{q}_{xy}$ [with magnitude $q_{xy} = \frac{2\pi}{\lambda}\sqrt{\cos^2(\alpha) + \cos^2(\beta) - 2\cos(\alpha)\cos(\beta)\cos\theta}$] the parallel part of the scattering vector $\mathbf{q} = \mathbf{k}_{\rm out} - \mathbf{k}_{\rm in}$ relative to the sample surface.

electron density profile (EDP) was resolved by XRR measurements. In addition, first systematic x-ray diffuse scattering (XDS) measurements from a liquid metal-liquid electrolyte interface were carried out providing *in situ* surface tension measurements for the system.

## II. THEORY

### A. X-ray scattering theory

The x-ray scattering geometry from a liquid-liquid interface spanning the $(x,y)$ plane is shown in Fig. 1. To aid the reader the relevant x-ray scattering theory and the distorted crystal model [3,16] both developed elsewhere will be presented briefly. This short overview is to aid understanding of the model description used in this paper. The differential cross section for scattering x rays with a scattering vector $q = (q_{xy}, q_z)$ from this interface, assumed for generality to be decorated by capillary waves, and to have some intrinsic interface-normal structure defined by the structure factor $\phi(q_z)$, is given by [18,27]

$$\frac{1}{A_0}\left(\frac{\mathrm{d}\sigma}{\mathrm{d}\Omega}\right) = \left(\frac{q_c}{2}\right)^4 \frac{T(\alpha)T(\beta)}{4\sin(\alpha)q_z^2}|\phi(q_z)|^2 \frac{\eta q_{\max}^{-\eta}}{2\pi q_{xy}^{2-\eta}}. \tag{1}$$

Here, $A_0, q_c, \alpha, \beta, T(\alpha)$, and $T(\beta)$ are, respectively, the illuminated interface area, the critical $q_z$ for total external reflection [18,27], the grazing angles of incidence and scattering of an x ray, and the transmission coefficients for these angles. $T(\alpha)$ and $T(\beta)$ enhance the intensity scattered near $q_c$, an effect known as the Yoneda peak [28]. $q_{\max} = \pi/a$, the upper wave vector cutoff of the capillary wave spectrum, is determined by the molecular radius $a$. $\eta = [k_B T/(2\pi\gamma)]q_z^2$ depends on the interfacial tension $\gamma$, and the temperature $T$, $k_B$ being the Boltzmann factor. Within the Born approximation and for a typical experimental XRR setup such as ours [18,27,29] the structure factor $\phi(q_z)$ is related to the interface-normal EDP, $\rho(z)$, by

$$|\phi(q_z)|^2 = \left|\frac{1}{\rho_{\rm Hg} - \rho_{\rm H_2O}} \int \mathrm{d}z \frac{\mathrm{d}\rho(z)}{\mathrm{d}z} \exp(iq_z z)\right|^2, \tag{2}$$

where $\rho_{\rm Hg}$ and $\rho_{\rm H_2O}$ are the bulk electron densities of mercury and water, respectively.

The intensity measured by a detector at some angular position $(\beta,\theta)$ corresponding to a scattering vector $q$, is the integral of Eq. (1) over the resolution function of the detector. At the specular condition $q_{x,y} = 0\,\text{Å}^{-1}$ (i.e., $\alpha = \beta$, $\theta = 0$), the detector measures the XRR, which is given by [18,27,29]

$$\frac{R(q_z)}{R_F(q_z)} = |\phi(q_z)|^2 \frac{\eta}{2\pi q_{\max}^{\eta}} \iint_{\Delta q_{xy}} \frac{1}{q_{xy}^{2-\eta}} \mathrm{d}q_{xy} \tag{3}$$

$$= |\phi(q_z)|^2 \exp\left(-q_z^2 \sigma_{\rm CW}^2(\Delta q_{xy})\right). \tag{4}$$

Here, $R_F$ is the Fresnel reflectivity from an ideally flat, smooth, and abrupt interface, and $\Delta q_{xy}$ is the detector's resolution function in the $q_{xy}$ plane. $\sigma_{\rm CW}$ is the CW-induced interface roughness. Off the specular condition the XDS is measured. Since XDS is very broadly distributed, a detector always picks up some of it. Thus, when measuring XRR, it is not possible to experimentally block the XDS and measure only the pure specularly-reflected x rays. Moreover, the XDS contribution is an integral over the resolution function, rendering this contribution, and hence the effective $\sigma_{\rm CW}$, resolution-dependent, as we indicated by the explicit notation $\sigma_{\rm CW}(\Delta q_{xy})$. When the interface includes some non-CW roughness, $\sigma_{\rm rms}$, Eq. (4) can be rewritten as

$$R(q_z)/R_F(q_z) = |\phi(q_z)|^2 \exp\left(-q_z^2 \sigma^2\right), \tag{5}$$

where $\sigma^2 = \sigma_{\rm rms}^2 + \sigma_{\rm CW}^2$ and $\phi(q_z)$ now denotes the roughness-free interface-normal structure factor.

### B. The distorted crystal model

The Hg-air and Hg-electrolyte interfaces were successfully modeled in previous studies [3,16,19,20,26] by the distorted crystal model (DCM), developed by Magnussen *et al.* [3,16]. In this model the liquid metal's interface-normal EDP is described by an infinite stack of layers with equal spacing $d$ and width $\sigma_n = \sqrt{n\sigma_b^2 + \sigma_i^2}$ of the $n$th layer, which increase with depth $z = nd$ below the surface at $z = 0$. Here, $\sigma_i$ is an intrinsic width, common to all layers, and $\sigma_b$ determines the rate by which $\sigma_n$ increases. The result is an oscillatory EDP of a progressively diminishing amplitude asymptotically approaching the bulk density of Hg $\rho_{\rm Hg}$ [3].

The extra dip in the Hg XRR curves can be accounted for within this model in two different ways. First, by adding a low-density adlayer at the interface, as done in previous studies [3,16,19,20], based on early simulations [30]. The adlayer is represented by a Gaussian of an amplitude $\rho_{\rm ad}$ and width $\sigma_{\rm ad}$, positioned at $z_{\rm ad}$ above the interface. The EDP of this adlayer model is thus given by

$$\rho(z) = \sum_{n=0}^{\infty} d \frac{\rho_{\mathrm{Hg}}}{\sigma_n \sqrt{2\pi}} \exp\left(-\frac{(z-nd)^2}{2\sigma_n^2}\right) + d_{\mathrm{ad}} \frac{\rho_{\mathrm{ad}}}{\sigma_{\mathrm{ad}}\sqrt{2\pi}} \exp\left(-\frac{(z-z_{\mathrm{ad}})^2}{2\sigma_{\mathrm{ad}}^2}\right) + \frac{\rho_{\mathrm{H_2O}}}{2}\left(1-\mathrm{erf}\left(\frac{z-z_{\mathrm{H_2O}}}{\sigma_{\mathrm{H_2O}}\sqrt{2}}\right)\right), \tag{6}$$

with $d_{\mathrm{ad}}$ fixed at 1 Å.

Newer simulations [31,32] do not support the presence of an adlayer but rather suggest that the first Hg layer is modified [33]. This modification is implemented here by starting the sum in the first term of Eq. (6) at $n = 1$ and describing the Hg surface layer ($n = 0$) by a Gaussian with an amplitude $\rho_{fi}$ at position $z_{fi}$ near $z = 0$ Å. The width of this Gaussian is set equal to $\sigma_i$, reducing the number of free parameters, since letting it vary in the fits yields near-zero values and does not improve the fit quality. The EDP of this modified-first-layer model is thus given by

$$\rho(z) = \sum_{n=1}^{\infty} d \frac{\rho_{\mathrm{Hg}}}{\sigma_n \sqrt{2\pi}} \exp\left(-\frac{(z-nd)^2}{2\sigma_n^2}\right) + d \frac{\rho_{fi}}{\sigma_i\sqrt{2\pi}} \exp\left(-\frac{(z-z_{fi})^2}{2\sigma_i^2}\right) + \frac{\rho_{\mathrm{H_2O}}}{2}\left(1-\mathrm{erf}\left(\frac{z-z_{\mathrm{H_2O}}}{\sigma_{\mathrm{H_2O}}\sqrt{2}}\right)\right). \tag{7}$$

For both adlayer and first-layer models, all Hg terms in the equations above were convoluted with the normalized atomic form factor of the Hg atom [16]. In both Eqs. (6) and (7) the last term accounts for the electrolyte side of the interface [19,26]. While its position $z_{\mathrm{H_2O}}$ was varied in the fit, its width, $\sigma_{\mathrm{H_2O}}$, was fixed at 0.66 Å, as its value had very little impact on the XRR fit, and when allowed to vary yielded unphysical, near zero, values.

The physical difference between the two models is illustrated in Fig. 2. Obviously, the different EDPs produce almost identical fits to the measured XRR curves over the experimentally accessible $q_z$ range. Although the two models are mathematically similar, it will be shown below that the different limitations in parameter space will result in different levels of acceptability of the values refined for some of the parameters.

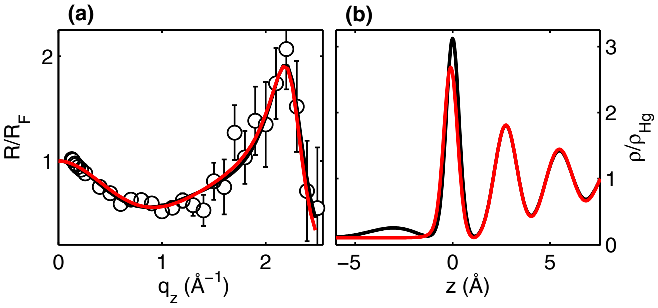

FIG. 2. Comparison of the interface region of the adlayer (black line) and first-layer (red line) model. (a) Surface structure factor fit to data, (b) corresponding electron density.

## III. EXPERIMENTAL

### A. Cell and samples

The cell, based on a previous room temperature design [19,26], was developed to allow *in situ* temperature-dependent x-ray scattering studies of the Hg-electrolyte interface simultaneously with electrochemical measurements (see Ref. [34]). It includes a PCTFE trough for the sample and 0.1 mm thick glass windows for entry and exit of the x rays. The temperature was measured with two Pt-100 elements. One was embedded in the PCTFE cell and separated from the Hg by only 0.5-mm PCTFE. The other resided in a glass tube, inserted into the electrolyte and positioned ≈5 mm above the interface. The temperature of the interface was taken as the mean value of the two. Heating and cooling of the sample was performed with a Peltier element underneath the sample trough, which was mounted on a water cooled copper block. Using this setup, the temperature was controlled within ±0.5 °C by a Lakeshore Model 340 temperature controller.

All parts of the assembly, which come into contact with the Hg or the electrolyte, were cleaned in Caro's acid ($H_2SO_5$) and rinsed with Milli-Q water. The PCTFE trough resides in a tightly sealed stainless steel cell, filled with high purity (>99.9996%) nitrogen gas before introducing the Hg and the electrolyte into the cell via glass tubes from reservoirs located above the cell.

All studies in this work were performed with 0.01 M NaF electrolyte, prepared from 99.995% pure NaF and Milli-Q water. The potential was controlled with a potentiostat (Solartron, Modulab) and a $Hg/Hg_2SO_4$ reference electrode (Schott). Differential capacitance measurements indicated that the potential of zero charge (PZC) of the system was $\Phi_{\mathrm{PZC}} \approx -0.85$ V, in good agreement with the literature [35].

### B. X-ray measurements

The measurements were carried out at an x-ray energy of 25 keV at the high-resolution beamline P08 [36] of the PETRA III synchrotron source at DESY (Hamburg, Germany) using the LISA liquid surface diffractometer [37,38]. The special geometry of the diffractometer allows varying the x-ray's incidence angle without moving the sample, thus avoiding movement-associated disturbances to the fragile liquid-liquid interface. Pickup of vibrations from the environment was virtually eliminated by mounting the cell on an active vibration isolation unit (Table Stable Ltd., TS-150), which itself is mounted on an isolated sample stage. A vertically oriented Mythen detector with 1280 50 $\mu$m-high elements was employed [39], allowing simultaneous measurements of a range of exit angles $\beta$ with a resolution of $\sim 4.4 \times 10^{-5}$ rad.

XRR and XDS data were taken in the geometry shown in Fig. 1. In the XRR measurements, the background due to the electrolyte and the Hg bulk scattering was measured by offsetting the detector to $\theta = \pm 1.2 \times 10^{-3}$ rad [Fig. 3(a)] or $\theta = \pm 8.7 \times 10^{-3}$ rad [Figs. 3(c) and 4(a)], and subtracted from the specular signal. The incident-beam-defining slits

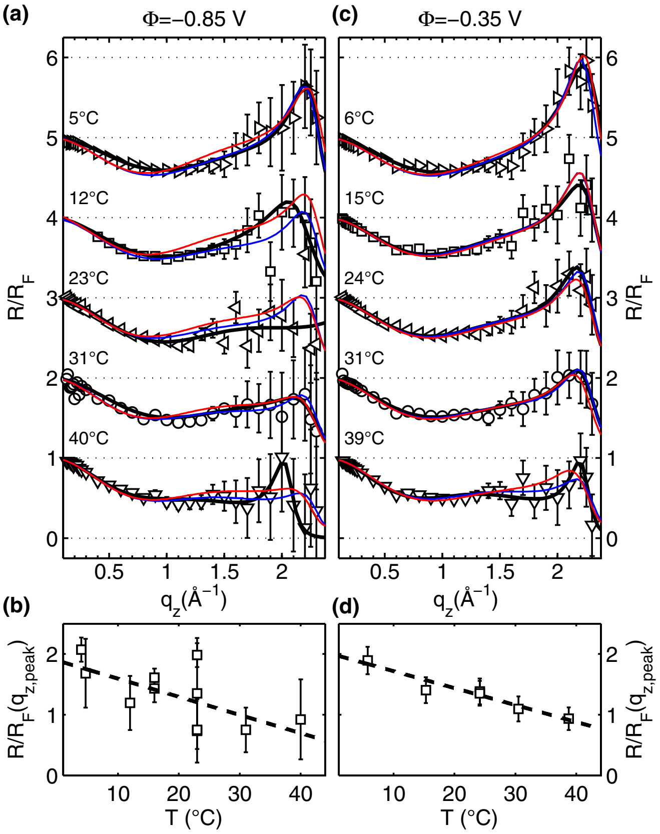

FIG. 3. XRR measurements of the interface between liquid Hg and 0.01 M NaF at potentials of (a) −0.85 and (c) −0.35 V at different temperatures between 4 to 40 °C. Curves have been shifted for clarity. The lowest $R/R_F$ curves have the original scale. The lines are fits to the data with the first-layer model. Black: fits of the individual data without parameter constraints. Blue: fits of the individual data with enforced relation between parameters. Red: multidimensional fitting method. (b) and (d) Height of the pseudo-Bragg peak (from individual data fits).

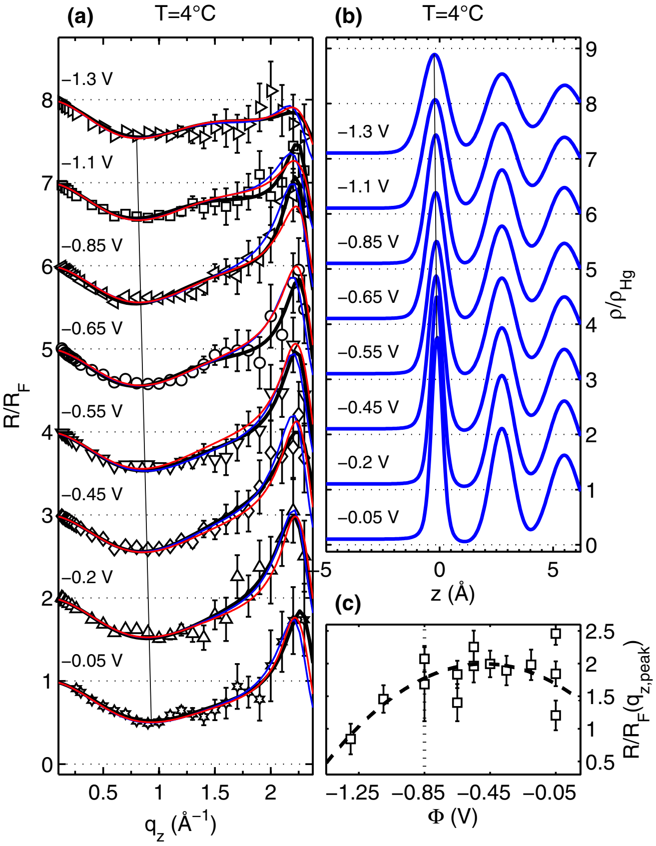

FIG. 4. (a) XRR measurements at a temperature of 4 °C and different potentials between −1.3 to −0.05 V. Curves have been shifted for clarity. The lowest $R/R_F$ curves have the original scale. The lines are fits as in Fig. 3. The thin vertical line indicates the shift in the minimum of $R/R_F$ at low $q_z$. (b) Electron densities corresponding to the blue lines. The thin vertical line indicates the shift of the position of the first layer. (c) Height of the pseudo-Bragg peak (from individual data fits).

were optimized to keep the illuminated area within the flat part of the Hg sample. The horizontal detector slit was set to an angular acceptance of $8.8 \times 10^{-4}$ rad. A virtual vertical detector slit could be defined by choosing the desired number of Mythen elements. The plots shown are integrated over 100 channels giving an effective vertical resolution of $4.4 \times 10^{-3}$ rad.

## IV. RESULTS

### A. Data overview

Two series of temperature dependent XRR curves were recorded between $T = 4\,^{\circ}\mathrm{C}$ and $40\,^{\circ}\mathrm{C}$ at $\Phi = -0.85$ V, i.e., at the PZC, and $\Phi = -0.35$ V. A selection of $R/R_F$ curves is shown in Figs. 3(a) and 3(c), with 3(b) and 3(d) showing the temperature dependence of the quasi-Bragg peak's height. As can be seen, at both Φ the height increases similarly towards lower temperatures, as expected from the resultant lowering of the CW roughness.

The potential dependent behavior was characterized by a series of XRR curves recorded at potentials between $\Phi = -0.05$ and $-1.3$ V at $T = 4\,^{\circ}\mathrm{C}$ [Fig. 4(a)]. Here, the highest quasi-Bragg peak is found at $\Phi = -0.48$ V [Fig. 4(c)], as observed also by Elsen *et al.* at room temperature [19]. This is in contradiction to pure CW theory, as the maximum should occur at the PZC where the surface tension is the highest. Together with the almost identical thermal gradients of the peak heights [Figs. 3(b) and 3(d)] it can be inferred, that the highest quasi-Bragg peak occurs at the found shifted potential of $\Phi = -0.48$ V over the whole temperature range measured. Additionally, as can be seen in Fig. 4(a), the minimum in the $R/R_F$ curves shifts to higher $q_z$ values with increasing potential (as shown by the thin black line). This indicates a systematical modification with Φ of the near interface region [as shown by the thin black line in Fig. 4(b)].

XDS measurements were carried out directly after each XRR, under identical $T$ and Φ. A typical XDS measurement with the specular peak at $q_z = 0.3$ Å$^{-1}$ in in-plane geometry (vertically aligned detector) is shown in Fig. 5(a) and a series of XDS measurement as a function of $q_{xy}$ in Fig. 5(b). The shape of the central peak at $q_{xy} \leqslant 5 \times 10^{-5}$ Å$^{-1}$ is dominated by the specular reflection and hence by the shape of the incident x-ray beam. At larger $q_{xy}$ the scattering by the capillary waves dominates and all measurements show the expected capillary

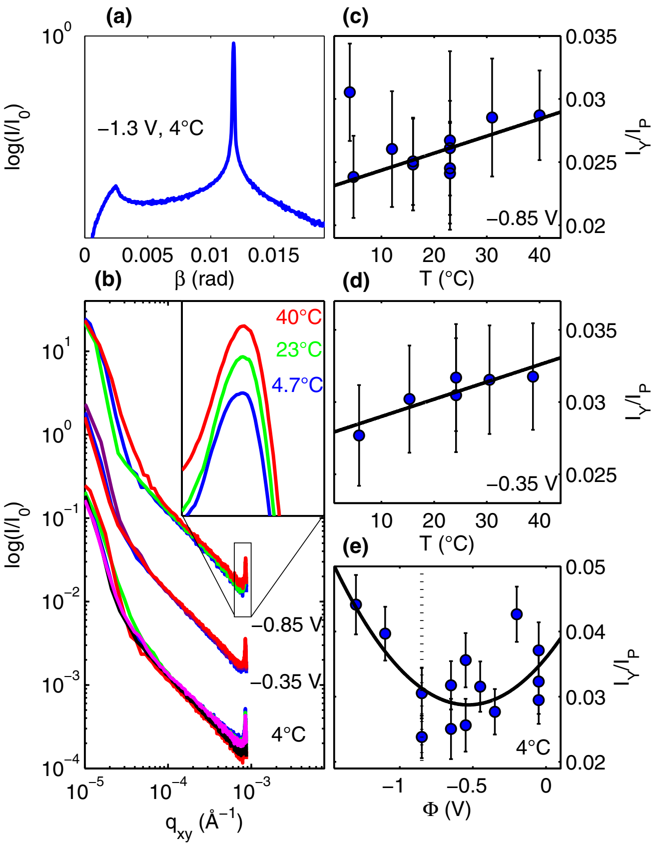

FIG. 5. (a) Example XDS measurement in angular coordinates. (b) Extracted $I(q_{xy})$ dependence of liquid Hg in 0.01 M NaF (for clarity the curves are offset by a factor of $10^{-4}$). The curves have been normalized by the integrated intensity of the specular peak at $q_z = 0.3$ Å$^{-1}$. Inset: Magnification of the Yoneda peaks at $q_{xy} \approx 10^{-3}$. (c)–(e) Integrated intensity [$q_{xy} = (8.59 \pm 0.23) \times 10^{-2}$ Å$^{-1}$] of the Yoneda peaks as a function of temperature and potential.

wave power law behavior. The small peaks at $q_{xy} \approx 10^{-3}$ Å$^{-1}$ are the Yoneda peaks, where $\beta = \alpha_c$ with $\alpha_c$ being the critical angle of total external reflection [18,27]. The peaks exhibit small, but clear, systematic variation with temperature and potential [Fig. 5(b), inset]. To illustrate these changes, the integrated intensity of the Yoneda peak in the XDS data, normalized by the integrated intensity of the central peak at $q_{xy} = 0$ are plotted as a function of temperature and potential in Figs. 5(c)–5(e). A (linear) increase with temperature is observed, in line with the decrease in the quasi-Bragg peak intensity, and the increase in the CW-dominated XDS. The potential dependence is parabolic as expected from the electrocapillary effect [19,26]. The minimum is also shifted to more positive potentials as for the quasi-Bragg peak height. However, the minimum is only at a potential of $\Phi = -0.53$ V and the shift is considerably smaller if the diffuse scattering at negative $q_{xy}$ values is examined. A quantitative analysis of these results is presented in the next sections.

### B. Analysis

In principle, the intrinsic interface-normal density profile, $\rho(z)$, unmodified by CW effects, can be obtained by fitting the measured $R/R_F$ curves by Eq. (3), using one of the DCM models in Sec. II B to calculate $\phi$. The fit will yield the best values for the $\rho(z)$-defining parameters. In practice, however, the models includes six (first-layer model : $\sigma_i$, $d$, $\sigma_b$, $\rho_{fi}$, $z_{fi}$, $z_{\mathrm{H_2O}}$) or seven (adlayer model : $\sigma_i$, $d$, $\sigma_b$, $\sigma_{\mathrm{ad}}$, $\rho_{\mathrm{ad}}$, $z_{\mathrm{ad}}$, $z_{\mathrm{H_2O}}$) parameters, some of which are likely to be weakly or strongly correlated with each other. Such correlations inhibit a robust fit, and result in large uncertainties in the derived parameter values, which, in turn, may mask $T$- and $\Phi$-dependent trends in the data. This is particularly true in our case, where diffuse and specular scattering are intermixed at all $q$ positions and are not easily separable [8,18,29,40], and the trends sought are expected to be subtle. While fixing the values of some of the parameters should reduce correlations between parameters, it may also distort $T$- and $\Phi$-dependent trends in the other fitted parameter values and in the derived $\rho$.

To avoid the pitfalls outlined above, the following analysis strategy was adopted which is composed of three consecutive fitting rounds, e.g., a free fit (FF), a correlation-corrected fit (CCF) and a multidimensional fit (MF). These will briefly be described here. For a more detailed description see Ref. [34].

(FF) Each raw XRR curve measured was used to generate 40 different $R/R_F$ curves by summing the intensities recorded in a varying number of detector pixels. The number of pixels corresponds therefore to a specific resolution $\Delta q_{xy}$, which is used in Eq. (3). Next, all these virtual $R/R_F$ curves, after subtracting the bulk liquid scattering background, were fitted by Eq. (3) for both $\rho$ models and with all parameters free to vary. Additionally, a multiplication factor $Amp0$ was fitted for data normalization. Scatter plots were then generated from the best-fit parameter values for all possible combinations of parameter pairs. An examination of these scatter plots indicated that all *significant* correlations between fit parameters result from an underlying identical dependence on $T$ and $\Phi$, rather than from a direct correlation between the parameters (for details see Ref. [34]).

(CCF) By linear fitting of the scatter plots, which showed a correlation and enforcing the obtained linear relation between the according parameters in this fitting round, the underlying $T$ and $\Phi$ dependence turned out to be linear to first order, within the scatter of the parameter values obtained.

(MF) To examine a linear behavior for parameters where the scatter plots did not yield good fits, the linear behavior was included *a priori* in this fitting round. Here, the thermal and potential gradients of the individual parameters were fitted rather than the parameters directly. For that the reflectivities for a fixed potential ($\Phi = -0.35$ V) or fixed temperature ($T = 4\,^\circ$C) were combined into a single data set, where every point has three coordinates, namely $q_z$, $T$, and $\Phi$. The whole data set was fitted with a surface structure factor of the form

$$|\phi(q_z,T,\Phi)|^2 = |\phi(q_z,d(T,\Phi),\sigma_i(T,\Phi),\sigma_b(T,\Phi),\cdots)|^2, \tag{8}$$

where we have constrained each fit parameter $P$ to depend linearly on $T$ and $\Phi$:

$$P(T,\Phi) = P_0 + P_T T - P_\Phi \Phi. \tag{9}$$

In this approach, the number of parameters employed to fit the entire data set is reduced to three times the number required to fit an individual $R/R_F$ curve (not counting $Amp0$ for each curve which were also fitted), yielding a more robust fit and lower parameter value uncertainty. This allows for a significantly more reliable determination of the individual $T$ and $\Phi$ dependencies of the interface structure.

To determine how CWs modify the intrinsic interfacial structure, a procedure similar to that used for the XRR above was adopted for the XDS scans. See Ref. [34] for further details. Thus a resolution volume was chosen by selecting a number of detector pixels, and the recorded XDS data were binned over such intervals. The resultant XDS curve was then fitted by integrating Eq. (1) over each detector pixel, convoluting the resultant curve with the shape of the incident beam, which was measured prior to the XDS measurement, and finally binning it over the same intervals. This was done for several resolution volumes, and the results were averaged.

### C. Fit results

For the XDS fits the value of $|\phi(q_z)|^2$ was taken from a fit of the associated XRR, where all parameters where allowed to vary freely and in which the value of $\gamma$ was set to the literature values [35]. Since in this case only the shape of $|\phi(q_z)|^2$ mattered and not the structure of $\rho(z)$, only the adlayer model was used. The XDS measurements at a large $q_z = 0.9\ \text{Å}^{-1}$ were used to minimize the beam's footprint and the consequent surface curvature effects. The interfacial tension $\gamma$ obtained (through $\eta$) from the XDS fits by Eq. 1 are shown in Fig. 6(a). The values are in reasonable agreement with the electrochemical measurements in Ref. [35]. Refitting the XRR curves using the $\gamma$ values obtained from the XDS fits influenced the quality of the results only marginally.

The XRR fit results for the individual $R/R_F$ curves are summarized in Figs. 6(b)–6(e). As mentioned above in the first round of fits all parameters were free to vary [results for first-layer model: black lines in Figs. 3(a), 3(c), and 4(a)]. The results for $\sigma_i$, the only parameter which was not constant within the errors but showed systematical variation, i.e., a linear behavior with $T$ and $\Phi$, are shown in Fig. 6(b) for both the adlayer and first-layer models. The values plotted are the means of the values obtained for the series of different resolutions at each $T$ and $\Phi$.

As discussed above, the scatter plots from this first fit round were analyzed for correlations and the following relations were obtained for the adlayer model:

$$z_{\mathrm{ad}}(\sigma_{\mathrm{ad}}) = -0.53\,\sigma_{\mathrm{ad}} - 2.34\ \text{Å},$$

$$\rho_{\mathrm{ad}}(\sigma_{\mathrm{ad}}) = (0.19\,\sigma_{\mathrm{ad}}/\text{Å} + 0.27)\rho_{\mathrm{Hg}},$$

and for the first-layer model:

$$z_{fi}(\rho_{fi}) = (-1.68\,\rho_{fi}/\rho_{\mathrm{Hg}} + 1.4)\ \text{Å}.$$

These relations were enforced in the next round of XRR fits, reducing the number of free parameters that describe the adlayer or the first layer to one, namely, $\sigma_{\mathrm{ad}}$ or $\rho_{fi}$. The parameters for which no correlations were indicated by the scatter plots analysis were fixed to their mean values. $\sigma_i$ did show some correlations, but no relations were fixed, to not impose its linear $T$ and $\Phi$ behavior as seen in Fig. 6(b) onto the other parameters. The present round of fits yielded an excellent agreement with the measured $R/R_F$ curves [fit results for first-layer model: blue lines in Figs. 3(a), 3(c), and 4(a)]. The unrestricted fit parameters, $\sigma_i$, $\sigma_{\mathrm{ad}}$ and $\rho_{fi}$, shown in Figs. 6(c)–6(e), exhibit now a clear linear dependence on $T$ and $\Phi$.

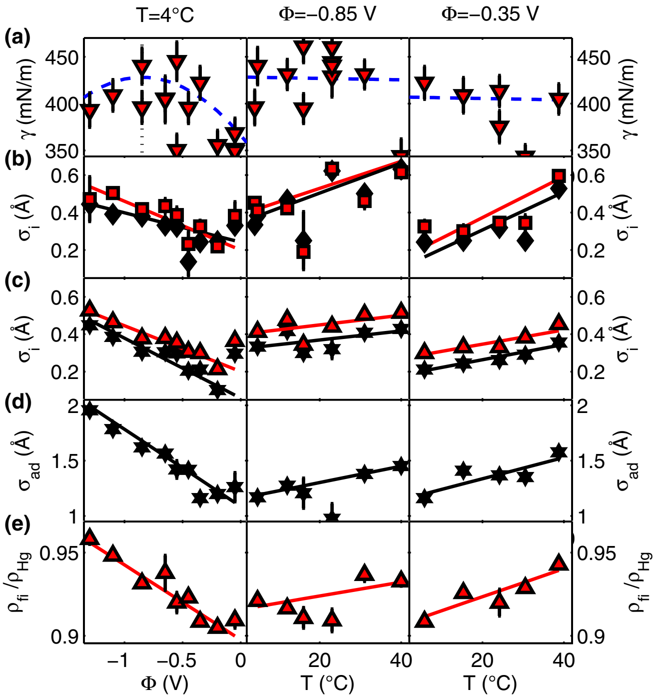

FIG. 6. (a) Plot of the surface tension $\gamma$ extracted from XDS measurements at $q_z = 0.9\ \text{Å}^{-1}$. The blue dashed lines correspond to the electrochemical data from [35]. (b) Results of the XRR fits for the parameter $\sigma_i$, averaged over the different $\Delta q_{xy}$ resolutions. Black: adlayer model. Red: first-layer model. Lines are linear fits. (c)–(e) Results of the XRR fits with enforced relation between parameters (see Sec. IV B), averaged over the different $\Delta q_{xy}$ resolutions. The temperature and potential dependence of the remaining free fit parameters within the adlayer model (black) and the first layer model (red) can be seen. Lines are linear fits.

It is important to note that the enforced linear relations would have also allowed $\sigma_{\mathrm{ad}}$ or $\rho_{fi}$ to remain constant, or show the same unsystematic behavior as in the preceding fitting round, over the whole $T$ and $\Phi$ ranges explored. Thus we see that our analysis method effectively reduces the uncertainties in the results and shows that linear $T$ and $\Phi$ dependencies are present in more parameters than just $\sigma_i$.

Next, such a linear dependence on $T$ and $\Phi$ was assumed for all parameters in the multidimensional fitting procedure. To determine the coefficients $P_T$ or $P_\Phi$ of these linear dependencies [Eq. (9)] an iterative approach was employed where in each iteration step the $P_T$ or $P_\Phi$ having the smallest relative error among the free-fit parameters was fixed to its obtained values for the rest of the iteration steps. Here again, a mean value and a mean error have been used, obtained by averaging results with different resolutions $\Delta q_{xy}$. This was repeated until all $P_T$ and $P_\Phi$ of the parameters were fixed (see Table I). Although the still-unfixed parameter values did change in the iteration following the fixing of a parameter, the changes were small in all cases.

TABLE I. Results of the multidimensional fitting of all reflectivities for both electron density models. The error is the 99% confidence bound given by the fit routine (MATLAB 2013a). Only for the parameters shown in bold are the values within these errors ≠0.

**adlayer**

| $P$ | $P_0$ | ±99% | $P_\Phi$ | ±99% | $P_T$ | ±99% |
|---|---|---|---|---|---|---|
| $\sigma_i$ | **0.122** | **0.020** | **0.183** | **0.072** | **0.0051** | **0.0024** |
| $d$ | **2.726** | **0.012** | −0.021 | 0.025 | **0.0023** | **0.0009** |
| $\sigma_b$ | **0.425** | **0.008** | **0.069** | **0.028** | **0.0009** | **0.0007** |
| $\sigma_{\text{ad}}$ | **1.111** | **0.143** | **0.559** | **0.498** | 0.0039 | 0.0225 |
| $\rho_{\text{ad}}$ | **0.401** | **0.085** | 0.223 | 0.291 | 0.0016 | 0.0018 |
| $z_{\text{ad}}$ | **−3.141** | **0.188** | −0.025 | 0.218 | −0.0001 | 0.0045 |

**first layer**

| $P$ | $P_0$ | ±99% | $P_\Phi$ | ±99% | $P_T$ | ±99% |
|---|---|---|---|---|---|---|
| $\sigma_i$ | **0.170** | **0.033** | **0.224** | **0.086** | **0.0040** | **0.0035** |
| $d$ | **2.702** | **0.016** | −0.005 | 0.029 | **0.0020** | **0.0014** |
| $\sigma_b$ | **0.406** | **0.015** | 0.007 | 0.029 | **0.0009** | **0.0008** |
| $\rho_{fi}$ | **0.910** | **0.008** | **0.038** | **0.023** | −0.0001 | 0.0004 |
| $z_{fi}$ | **−0.119** | **0.014** | **−0.073** | **0.038** | −0.0002 | 0.0008 |

As demonstrated in Figs. 3(c) and 4(a) (red lines), the resulting final fit is in very good agreement with the reflectivity data, even for the curves not included in the fit [Fig. 3(a)]. Only a few of the $P_\Phi$ and $P_T$ parameters deviate from zero within the error limits (Table I bold values), i.e., indicate a significant dependence of the structural parameters on $T$ or $\Phi$. Similar fits where the nonsignificant $P_\Phi$ and $P_T$ were set to 0 from the beginning produced slightly different significant parameter values but still provided good fits to the measured $R/R_F$, with only minor deviations from the original fits (see Ref. [34]). This demonstrates the robustness of the applied fitting procedure.

As Table I demonstrates, the major effect of an increase in $T$ is an increase in the layer spacing $d$, accompanied by an increases in $\sigma_i$. In contrast, $d$ is not affected by changes in the potential $\Phi$. Rather, $\sigma_i$ is significantly changed. In addition, changes in $\Phi$ also influence those parameters that describe the immediate interface with the electrolyte solution, i.e., $\sigma_{\text{ad}}$ within the adlayer model and $\rho_{fi}$ and $z_{fi}$ within the first-layer model.

## V. DISCUSSION

The results from the systematic fits of the XDS data suggest, that the diffuse scattering is well described by CW theory at least in the $q$-range measured in our experiments. Thus an assignment of the anomalous $T$ and $\Phi$ behavior discussed in Sec. I to an anomalous $\gamma(T,\Phi)$ dependence is not supported by experiment.

All three XRR fitting methods, the individual fitting, the fitting with enforced relations between parameters and the multidimensional fitting show an increasing roughness with increasing temperature, independent of the model used. From this we conclude that this behavior is intrinsic to the surface of Hg. Additionally, the multidimensional fitting method showed an expansion of the vertical spacing $d$ between the atomic layers at the liquid metal surface of approximately 3% (from Table I) for both models. This behavior is far more than can be explained by a simple thermal expansion of the Hg bulk liquid, which is only ∼0.7% [41] in this temperature range. We therefore assign the increase in the Hg layer spacing with $T$ as well as the accompanying parallel broadening of these layers to a genuine interface effect. Apparently, the thermal increase in the atomic motion influences the stratification of the Hg into atomic layers. Although comparison to computer simulations is complicated due to the often small sample size used, an expansion of the layer spacing of Hg with temperature has been observed in such studies [33].

The effect of the potential on the interface structure noticeably differs from that of the temperature. The Hg interfacial region ($\sigma_{\text{ad}}$, $z_{fi}$, see Table I) broadens towards the electrolyte with decreasing potential. This effect occurs in both models and is consistent with former results. In the study by Elsen *et al.*, this behavior was attributed to contributions of the conduction electrons to the total electron density profile [19]. These free electrons are polarized by the strong electric field in the electrochemical double layer at the electrode surface according to the theory by Schmickler and Henderson [24]. The magnitude of the effect predicted by this theory for Hg electrodes is in good agreement with the x-ray reflectivity data [19]. The increase in electron surface density towards more negative potentials may also explain the increase in electron density of the first layer $\rho_{fi}$ found in the first-layer model (Table I). Possible contributions to this effect may come from a concomitant increase in the packing density of the Hg ion cores, which would be expected from electrostatic arguments (increased lateral screening of the electronic charge).

More puzzling is the change of $\sigma_i$ with $\Phi$, which is not accompanied by a change of the layer spacing $d$. Therefore such a change cannot be assigned to an increased atomic motion as with the temperature dependent effect. Also an increased screening of the electronic charge in the bulk, which would allow the ion cores to move closer to each other, seems unlikely, since the negative charge is expected to accumulate at the interface. In our analysis, the roughness is given by a sum in quadrature of $\sigma_i$ and $\sigma_{\text{CW}}$. The later is determined from the surface tension using CW theory. However, at atomic dimensions, i.e., the length scale of the layering phenomena, which were not covered by our XDS measurements, this continuum theory may break down, leading to additional contributions to the roughness. Such an enhanced short-range roughness is likely to be influenced by a potential induced change of the surface region as observed in our studies. This may cause an increasing $\sigma_{\text{rms}}$ as in Eq. (5), which would not be distinguishable from an increase in $\sigma_i$. Additionally, if this roughness is correlated over a significant length scale it would cause an increased diffuse scattering intensity at large $q_{xy}$. This has indeed been observed for the free surface of water and several other liquids [42,43] and can be accounted for by a wave vector dependent surface tension [44], which has a reduced value for the corresponding length scales. This could be the cause of the observed potential dependent roughness deviation, since the observed increase in the electron density of the first layer would most likely significantly influence such small scale roughness phenomena.

Some of the previous theoretical studies used an analysis, which eliminated the influence of $\sigma_{\mathrm{rms}}$ and gave access to the "intrinsic surface" of the simulated system [45], which is closely related to $\rho(z)$. These studies suggest that for simple liquids at the smallest length scales the surface tension hydrodynamics breaks down completely and a transition to a molecular diffusion regime takes place [46]. This may also account for the roughness anomaly of the surface structure of Hg. Unfortunately, to our knowledge, there exists no theoretical work for the Hg surface, which applies this scheme and could shed more light on the underlying mechanisms which cause the surface of Hg to differ from all other liquid metals.

Overall, the first-layer model seems preferable to the adlayer model, since the theoretical work it is based on Ref. [33] helps to explain the underlying physics. Furthermore, additional theoretical [31] and experimental [47] works suggest that the first of the Hg layers at the vapor interface is expected to be quite different from the second and underlying layers, which behave just like the bulk liquid.

## VI. SUMMARY

In this work, we presented combined x-ray reflectivity and x-ray diffuse scattering measurements of the deeply buried liquid-liquid interface between Hg and a NaF (0.01 M) electrolyte solution. In addition to a comprehensive study of the influence of temperature and potential on the interface structure at the atomic scale, new methodological approaches were investigated. The following results were obtained. (1) All reflectivity curves in the studied temperature and potential regime (4 °C to 40 °C, −1.3 to −0.05 V) exhibit a pseudo-Bragg peak, indicating surface layering within the Hg phase. The amplitude of this peak varies with $T$ and $\Phi$. (2) Measurements of the XDS resulting from liquid-liquid interfaces were performed. The obtained data are in good agreement with the variation of the surface tension with $T$ and $\Phi$ from literature [35]. (3) The temperature dependent XRR data showed the temperature anomaly of the Hg surface roughness [16] to persist at the Hg-electrolyte interface. (4) By including a linear $T$ and $\Phi$ dependence of the parameters in a multidimensional fit, several reflectivities could be fitted simultaneously. The obtained fit requires explicit changes with $T$ and $\Phi$ only for selected parameters and satisfactorily describes the entire data set over the full range of the environmental parameters employed in this study. (5) Our results uncover a hitherto unobserved expansion of the near-surface layer spacing, well beyond the normal bulk thermal expansion. (6) Changing the potential towards more negative values primarily causes a broadening of the Hg-electrolyte interface towards the electrolyte. This is in agreement with an explanation of this effect by the electronic polarization at the interface as predicted by the Schmickler-Henderson theory [19,24]. As indicated by these results, x-ray scattering studies employing modern instruments at third generation synchrotron sources enable detailed investigations of liquid-liquid interfaces on the atomic scale.

## ACKNOWLEDGMENTS

We gratefully acknowledge financial support by the Bundesministerium für Bildung und Forschung, Germany (Projects 05K10FK2 and 05KS7FK3), the U.S. Department of Energy, Division of Materials Science under Contract No. DE-SC0012704 (B.O.) and the United States - Israel Binational Science Foundation, Jerusalem (M.D.), and thank the beamline staff of P08 at PETRA III, Deutsches Elektronen-Synchrotron, Germany for their experimental support.

---

[1] P. S. Pershan, J. App. Phys. **116**, 222201 (2014).

[2] S. A. Rice, Proc. Natl. Acad. Sci. USA **84**, 4709 (1987).

[3] O. M. Magnussen, B. M. Ocko, M. J. Regan, K. Penanen, P. S. Pershan, and M. Deutsch, Phys. Rev. Lett. **74**, 4444 (1995).

[4] M. J. Regan, E. H. Kawamoto, S. Lee, P. S. Pershan, N. Maskil, M. Deutsch, O. M. Magnussen, B. M. Ocko, and L. E. Berman, Phys. Rev. Lett. **75**, 2498 (1995).

[5] H. Tostmann, E. DiMasi, P. S. Pershan, B. M. Ocko, O. G. Shpyrko, and M. Deutsch, Phys. Rev. B **59**, 783 (1999).

[6] O. Shpyrko, P. Huber, A. Grigoriev, P. Pershan, B. Ocko, H. Tostmann, and M. Deutsch, Phys. Rev. B **67**, 115405 (2003).

[7] O. G. Shpyrko, A. Y. Grigoriev, C. Steimer, P. S. Pershan, B. Lin, M. Meron, T. Graber, J. Gerbhardt, B. Ocko, and M. Deutsch, Phys. Rev. B **70**, 224206 (2004).

[8] P. S. Pershan, S. Stolz, O. G. Shpyrko, M. Deutsch, V. S. K. Balagurusamy, M. Meron, B. Lin, and R. Streitel, Phys. Rev. B **79**, 115417 (2009).

[9] H. Tostmann, E. DiMasi, B. M. Ocko, M. Deutsch, and P. S. Pershan, J. Non Cryst. Sol. **250**, 182 (1999).

[10] N. Lei, Z. Huang, and S. A. Rice, J. Chem. Phys. **104**, 4802 (1996).

[11] M. J. Regan, P. S. Pershan, O. M. Magnussen, B. M. Ocko, M. Deutsch, and L. E. Berman, Phys. Rev. B **55**, 15874 (1997).

[12] D. Li, X. Jiang, B. Yang, and S. A. Rice, J. Chem. Phys. **122**, 224702 (2005).

[13] O. G. Shpyrko, R. Streitel, V. S. K. Balagurusamy, A. Y. Grigoriev, M. Deutsch, B. M. Ocko, M. Meron, B. Lin, and P. S. Pershan, Science **313**, 77 (2006).

[14] V. S. K. Balagurusamy, R. Streitel, O. G. Shpyrko, P. S. Pershan, M. Meron, and B. Lin, Phys. Rev. B **75**, 104209 (2007).

[15] P. S. Pershan, S. E. Stoltz, S. Mechler, O. G. Shpyrko, A. Y. Grigoriev, V. S. K. Balagurusamy, B. H. Lin, and M. Meron, Phys. Rev. B **80**, 125414 (2009).

[16] E. DiMasi, H. Tostmann, B. M. Ocko, P. S. Pershan, and M. Deutsch, Phys. Rev. B **58**, R13419(R) (1998).

[17] M. J. Regan, P. S. Pershan, O. M. Magnussen, B. M. Ocko, M. Deutsch, and L. E. Berman, Phys. Rev. B **54**, 9730 (1996).

[18] P. S. Pershan and M. L. Schlossman, *Liquid Surfaces and Interfaces* (Cambridge University Press, Cambridge, 2012).

[19] A. Elsen, B. M. Murphy, B. M. Ocko, L. Tamam, M. Deutsch, I. Kuzmenko, and O. M. Magnussen, Phys. Rev. Lett. **104**, 105501 (2010).

[20] J. F. L. Duval, S. Bera, L. J. Michot, J. Daillant, L. Belloni, O. Konovalov, and D. Pontoni, Phys. Rev. Lett. **108**, 206102 (2012).

[21] H. L. F. Helmholtz, Ann. Phys., Leipzig **243**, 337 (1879).

[22] G. Gouy, J. Phys. Theor. Appl. **9**, 457 (1910).

[23] D. L. Chapman, Philos. Mag. **25**, 475 (1913).

[24] W. Schmickler and D. Henderson, Prog. Surf. Sci. **22**, 323 (1986).

[25] A. I. Carim, S. M. Collins, J. M. Foley, and S. Maldonado, J. Am. Chem. Soc. **133**, 13292 (2011).

[26] A. Elsen, S. Festersen, B. Runge, C. T. Koops, B. M. Ocko, M. Deutsch, O. H. Seeck, B. M. Murphy, and O. M. Magnussen, Proc. Natl. Acad. Sci. USA **110**, 6663 (2013).

[27] J. Als-Nielsen and D. McMorrow, *Elements of Modern X-ray Physics* (John Wiley & Sons Ltd., West Sussex, 2001).

[28] Y. Yoneda, Phys. Rev. **131**, 2010 (1963).

[29] A. Braslau, P. S. Pershan, G. Swislow, B. M. Ocko, and J. Als-Nielsen, Phys. Rev. A **38**, 2457 (1988).

[30] M. F. D'Evelyn and S. A. Rice, J. Chem. Phys. **78**, 5081 (1983).

[31] D. S. Chekmarev, M. Zhao, and S. A. Rice, Phys. Rev. E **59**, 479 (1999).

[32] J.-M. Bomont, J.-L. Bretonnet, D. J. Gonzalez, and L. E. Gonzalez, Phys. Rev. B **79**, 144202 (2009).

[33] L. Calderin, L. E. Gonzalez, and D. J. Gonzalez, Phys. Rev. B **87**, 014201 (2013).

[34] See Supplemental Material at http://link.aps.org/supplemental/10.1103/PhysRevB.93.165408 for description of Hg cell and details of fitting proceedure.

[35] N. Cuong, C. V. D'Alkaine, A. Jenard, and H. D. Hurwitz, J. Electroanal. Chem. **51**, 377 (1974).

[36] O. H. Seeck, C. Deiter, K. Pflaum, F. Bertram, A. Beerlink, H. Franz, J. Horbach, H. Schulte-Schrepping, B. M. Murphy, M. Greve, and O. M. Magnussen, J. Synchrotron Radiat. **19**, 30 (2012).

[37] B. M. Murphy, M. Greve, B. Runge, C. T. Koops, A. Elsen, J. Stettner, O. H. Seeck, and O. M. Magnussen, AIP Conf. Proc. **1234**, 155 (2010).

[38] B. M. Murphy, M. Greve, B. Runge, C. T. Koops, A. Elsen, J. Stettner, O. H. Seeck, and O. M. Magnussen, J. Synchrotron Radiat. **21**, 45 (2014).

[39] A. Bergamaschi, A. Cervellino, R. Dinapoli, F. Gozzo, B. Heinrich, I. Johnson, P. Kraft, A. Mozzanica, B. Schmitt, and X. Shi, J. Synchrotron Radiat. **17**, 653 (2010).

[40] P. S. Pershan, J. Phys. Chem. **113**, 3639 (2009).

[41] D. Ambrose, Metrologia **27**, 245 (1990).

[42] C. Fradine, A. Braslau, D. Luzet, D. Smiligies, M. Alba, N. Boudet, K. Mecke, and J. Daillant, Nature (Nature) **403**, 871 (2000).

[43] S. Mora, J. Daillant, K. Mecke, D. Luzet, A. Braslau, M. Alba, and B. Struth, Phys. Rev. Lett. **90**, 216101 (2003).

[44] K. R. Mecke and S. Dietrich, Phys. Rev. E **59**, 6766 (1999).

[45] P. Tarazona and E. Chacon, Phys. Rev. B **70**, 235407 (2004).

[46] R. Delgado-Buscalioni, E. Chacon, and P. Tarazona, Phys. Rev. Lett. **101**, 106102 (2008).

[47] B. N. Thomas, S. W. Barton, F. Novak, and S. A. Rice, J. Chem. Phys. **86**, 1036 (1987).